JOURNAL OF THERMOPHYSICS AND HEAT TRANSFER
Vol. 25, No. 2, April–June 2011

Direct Numerical Simulation of the Turbulent Ekman Layer: Instantaneous Flow Structures

Scott Waggy, Stuart Marlatt,* and Sedat Biringen†
University of Colorado, Boulder, Colorado 80309

DOI: 10.2514/1.50858

A direct numerical simulation of the turbulent Ekman layer at a Reynolds number of 400 was performed. Two-point velocity and pressure correlations were plotted to identify and estimate the average sizes and locations of instantaneous flow structures characteristic of turbulence. It was found that these structures are characterized by elongated eddies near the surface, which broaden away from the wall. The correlations roughly align with the mean shear direction near the surface; moving away from the wall, they exhibit tilting and lifting of downstream segments. The u' two-point correlation, in particular, showed significant tilting in the outer regions of the flow demonstrating that this is a significant deviation from typical nonrotating boundary-layer behavior.

Nomenclature

L_x, L_y	=	domain length in x, y directions
p	=	pressure
p'	=	pressure perturbation
Q^+	=	magnitude of velocity in wall units
R_{ab}	=	autocorrelation between arbitrary variables a and b
Re	=	Reynolds number
Ro	=	Rossby number
u, v, w	=	streamwise, spanwise, and vertical velocity components
$u', \ldots$	=	streamwise (etc.) fluctuating velocity component
$u^+, \ldots$	=	streamwise (etc.) velocity in wall units
u_*	=	friction velocity
x, y, z	=	streamwise, spanwise, and vertical coordinates
z^+	=	vertical coordinate in terms of wall units
$\Delta x^+, \ldots$	=	streamwise (etc.) grid spacing in wall units
δ	=	neutral layer turbulent depth
δ_E	=	Ekman thickness
k	=	von Karman constant taken to be 0.41
λ	=	Taylor microscale
ν	=	kinematic viscosity
Ω	=	rate of rotation

I. Introduction

A BALANCE of pressure gradient and Coriolis forces are characteristic of the Ekman layer. The flow occurs when a steady, horizontally homogeneous shear flow is subject to system rotation (with respect to an inertial frame of reference). As a result of the three-dimensional mean flow, energy transfer by means of Coriolis redistribution results in complex interactions between velocity components. In this work, we expand on the results of Marlatt et al. [1], and analyze instantaneous turbulent structures generated by the neutrally stratified Ekman layer. Although neutral stratification rarely occurs in nature, the Ekman model is commonly regarded as an approximation of the atmospheric boundary layer (ABL). More frequently in nature, surface heating (or cooling) results in buoyancy forces. This work offers a baseline upon which thermally stratified cases can be compared.

Turbulent structures of the Ekman layer have been considered previously. Miyashita et al. [2] studied the evolution of material lines in the inner and outer regions of the flow. Their results showed that material lines near the wall were advected further in the spanwise direction than lines initially away from the wall. This is to be expected as the mean spanwise velocity tends toward zero in the outer layer. Le et al. [3] also analyzed three-dimensional structures created by impulsively moving the wall of a channel flow. Their analysis was completed by means of joint probability density functions and demonstrated that positive and negative vorticity respond differently in the flow such that turbulent structures lose any spanwise symmetry for 3-D boundary layers. Coleman provides an excellent analysis of Reynolds number effects for the Ekman flow [4]. His results showed that at an increased Reynolds number there was an increase in the discernable logarithmic region of the flow. Both the friction velocity and the angle of the surface shear stress are reduced with an increased Reynolds number.

Taylor and Sarkar compared direct numerical simulation (DNS) and large eddy simulation (LES) results for the Ekman layer with thermal stratification [5]. Their LES results compared well with DNS results when temperature was a passive scalar. However, underprediction of heat flux occurred when an outer layer stratification was imposed. Their work demonstrated that small-scale motions were not captured by the LES or represented in the applied subgrid-scale models. Direct simulation results indicate that it is these scales which are responsible for the entrainment of fluid into the boundary layer [5].

The goal of this work is to determine characteristic turbulent structures in the unstratified turbulent Ekman layer by analyzing instantaneous flow contours as well as two-point velocity and pressure autocorrelations. The present study avails new details of turbulence dynamics in rotating turbulent boundary layers especially in the near-wall region which, in turn, can be instrumental in the parameterization of turbulence in large-scale atmospheric boundary-layer models using time-averaged equations.

II. Governing Equations

Direct numerical simulation (DNS) of the turbulent Ekman layer fully resolves all relevant scales so that no turbulence model is necessary. This provides an opportunity to calculate turbulent statistics with high fidelity provided that the flowfield is sufficiently well resolved, hence limiting the Reynolds number achievable. The current DNS mathematical model is based on the full, unsteady, three-dimensional equations of motion for incompressible flows with system rotation about the z-axis in the inertial reference frame (Fig. 1). These are given in vector form below:

Presented as Paper 2010-1255 at the AIAA 48th Aerospace Sciences Meeting, Orlando, FL, 4–7 January 2010; received 20 May 2010; revision received 24 September 2010; accepted for publication 28 October 2010.

*Present address: United Launch Alliance, Littleton, Colorado 80120.
†Department of Aerospace Engineering Sciences (Corresponding Author).

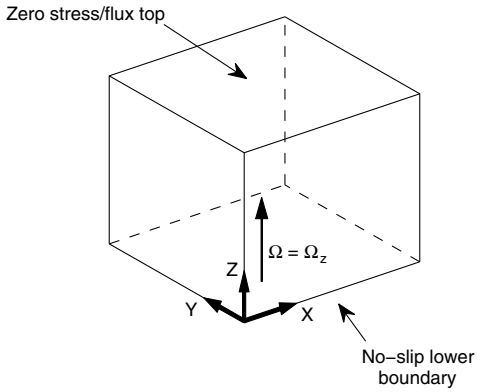

Fig. 1 Computational domain: periodic in x and y, no-slip at $z = 0$, stress free at $z = z_{\max}$.

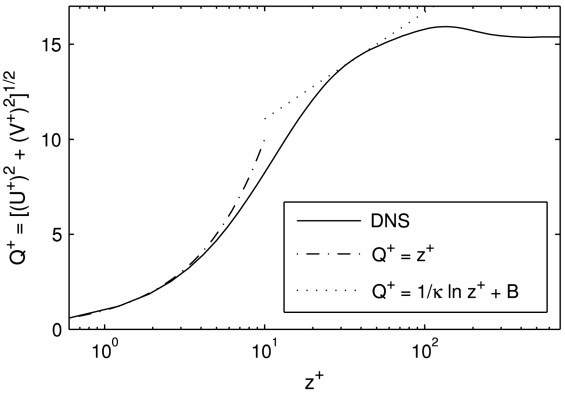

Fig. 2 Mean velocity profile in wall units along with inner-layer scaling and log law. For log law: $\kappa = 0.41$ and $B = 5.46$.

$$\nabla \cdot \mathbf{u} = 0 \tag{1}$$

$$\frac{\partial \mathbf{u}}{\partial t} + \mathbf{u} \cdot \nabla \mathbf{u} + \frac{1}{Ro}(-v\delta_{i1} + u\delta_{i2}) = -\nabla P + \frac{1}{Re}\nabla^2 \mathbf{u} \tag{2}$$

In the above equations, U_g is the geostrophic velocity, the Ekman depth (δ_E) is defined by $\delta_E = \sqrt{\nu/\Omega}$, ν is the kinematic viscosity, and Ω is the rate of rotation. The terms δ_{i1} and δ_{i2} refer to the Kronecker delta. The Reynolds number is defined as $Re = U_g\delta_E/\nu$ and the Rossby number is given by $Ro = U_g/2\Omega\delta_E$. Given the definition of the Ekman depth δ_E, the Reynolds and Rossby numbers are related by $Re = 2Ro$. The case presented here uses a Reynolds number of $Re = 400$ and (consequently) a Rossby number of $Ro = 200$. Self-sustaining turbulence can be generated at this Reynolds number; previous studies [4,6–8] have shown that at $Re = 400$ the Ekman flow exhibits an inertial subrange, which abides by the $-5/3$ scaling if only for a small range of wavenumbers.

III. Numerical Method

A schematic of the coordinate directions is given in Fig. 1. Note that the axis of rotation is aligned with the vertical z direction. The boundary conditions assume periodicity in the streamwise x and spanwise y directions. A no-slip condition is applied at $z = 0$ and an impenetrable stress-free lid is imposed at $z = z_{\max}$:

$$\left.\frac{\partial u}{\partial z}\right|_{\text{top}} = \left.\frac{\partial v}{\partial z}\right|_{\text{top}} = w_{\text{top}} = 0 \tag{3}$$

The DNS implements the third-order time-accurate fractional-step Runge–Kutta time integrator of Le and Moin [9]. Derivatives in the x and y directions are computed pseudospectrally; upstream biased finite differences (fifth-order) are used in the vertical direction. Code validation was confirmed by Marlatt and Biringen [10] by imposing perturbations obtained from the linear stability theory and tracking the phase and amplitude evolution of these waves. Results showed good agreement between the linear theory predictions and the growth of the velocity fluctuations calculated with the DNS model. Prior work using the present numerical model also shows excellent agreement between comparable studies [1,7].

In the current simulations for a domain of size $26\delta_E \times 26\delta_E \times 34\delta_E$, a uniform grid spacing of $\Delta x^+ = \Delta y^+ \approx 5.28$ was used in the x and y directions. An exponentially stretched and staggered grid was used in the vertical direction so that gridpoints were clustered near to the lower boundary. The spacing was such that $\Delta z^+_{\min} \approx 0.60$. It was determined previously that this resolution was sufficient to ensure the solution was mesh-independent [1].

The simulation was run till a quasi-steady state was reached based on the sum of the kinetic energy in the domain. A plot of the mean velocity in terms of wall units are provided in Fig. 2. The inner layer captured by the DNS is well represented by $Q^+ = z^+$ up until approximately $z^+ \approx 0.5$. In the outer layer, the low Reynolds number allows only a small region to abide by the log-law.

IV. Two-Point Correlations

In turbulent flow analysis, statistical methods offer a means of quantifying the structure and intensity of time dependent variables. For example, the two-point correlation offers insight into the shape and extent of turbulent structures. Given two arbitrary variables a and b, a two-point correlation between the two is defined as given by

$$R_{ab}(\Delta x, \Delta y, z_1, z_2) = \frac{\int_0^\tau \int_0^{L_y} \int_0^{L_x} a(x, y, z_1, t) b(x + \Delta x, y + \Delta y, z_2, t)\, \mathrm{d}x\, \mathrm{d}y\, \mathrm{d}t}{\tau L_x L_y a_{\text{rms}}(z_1) b_{\text{rms}}(z_2)} \tag{4}$$

This definition of the two-point correlation can be applied to both velocity and pressure fluctuations. The definition of the correlation is written in such a manner to emphasize that the results are averaged both spatially and temporally. The spatial integration limits of L_x and L_y imply that the entire x/y plane is averaged over for all values of x and y. The time interval over which the statistics are averaged is denoted by τ. In the present work, temporal averages were computed using approximately 200 evenly spaced time instances while the spatial averages were collected as averages over the horizontal (x, y) plane. Since the domain is periodic in both x and y directions and the boundary conditions on the top and bottom of the domain are not a function of x or y, this is a viable way of obtaining spatial averages for the present problem. The autocorrelation is also defined such that its value is $+1$ at $R_{ab}(0, 0, z_1, z_2)$ if $a = b$ and $z_1 = z_2$.

Two-dimensional projections of the autocorrelations provide a visualization of the turbulent structures throughout the domain.

V. One-Dimensional Correlations

Using the autocorrelation as defined in Eq. (4), a one-dimensional function can be formed if $z_1 = z_2 =$ constant and either $\Delta x = 0$ or $\Delta y = 0$. Results were obtained for $R_{u'u'}$, $R_{v'v'}$, $R_{w'w'}$, and $R_{p'p'}$. Figure 3 shows these four autocorrelations as a function of Δx for the nearwall region (a) and the far field (b). Note that the separation distance has been normalized by the turbulent depth $\delta = u_*/f$ where u_* is the friction velocity and f is the Coriolis parameter defined as $f = 2\Omega$.

The data from Fig. 3a is located within the region where the law of the wall (inner-layer) holds. The slow decay of the $R_{u'u'}$ correlation is the most prevalent feature of these results. A similar result to this was noted by Coleman et al. [6]. While the other three correlations tends to zero, the large streamwise structure is not fully captured within the domain. In a purely laminar flow, there would be no variation in the autocorrelation regardless of the separation. Thus, it is believed that the slow decay of the streamwise correlation is indicative of the viscous nature of the flow close to the wall.

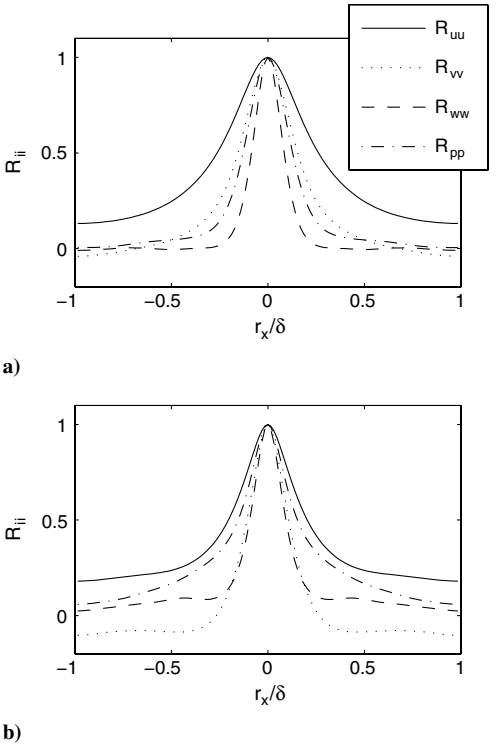

Fig. 3 Streamwise one-dimensional correlation: a) $z_1^+ = z_2^+ \approx 2.60$, and b) $z_1^+ = z_2^+ \approx 88.16$.

From these result presented in Fig. 3 we can calculate the Taylor microscale λ as defined by Eq. (5) [11]

$$\lambda(z_1^+) = \left[-\frac{1}{2}\frac{\mathrm{d}^2}{\mathrm{d}x^2} R_{u'u'}(0, 0, z_1^+, z_1^+) \right]^{-1/2} \tag{5}$$

Near the wall, $\lambda(z_1^+ = 2.60) \approx 0.17\delta$; in the far field, $\lambda(z_1^+ = 88.16) \approx 0.10\delta$. The contraction of the Taylor microscale moving away from the wall is to be expected as the derivative of the turbulent fluctuations in the streamwise direction scale as the inverse of the Taylor microscale. This shows that the gradient of the fluctuations increases moving further away from the boundary (where viscosity plays a smaller role in the dynamics of the flow).

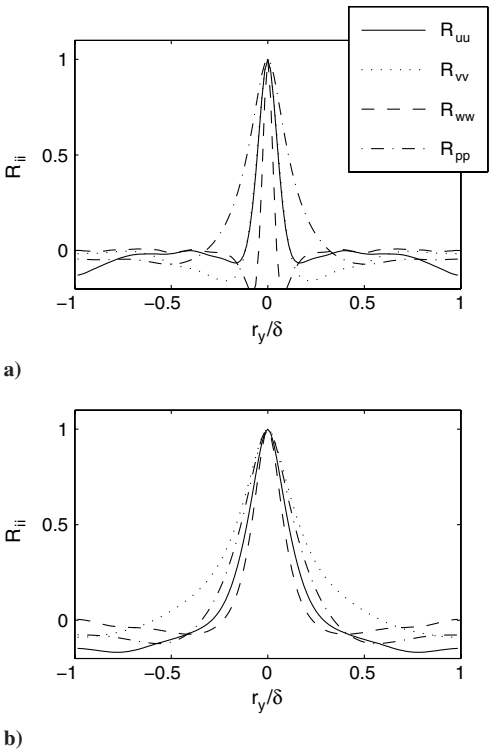

Fig. 4 Spanwise one-dimensional correlation: a) $z_1^+ = z_2^+ \approx 2.60$, and b) $z_1^+ = z_2^+ \approx 88.16$.

While the vertical velocity correlation and the pressure correlation tend towards zero at increased spacing, Fig. 3a shows that the spanwise velocity displays an unusual negative correlation as large spacings. This is amplified moving further into the boundary layer as the correlation holds steady at a value of approximately -0.08 for all $|r_x/\delta| > 0.35$.

The same correlations are shown in Fig. 4 with a spanwise separation. It is clear that the velocity autocorrelations are much narrower in the spanwise direction than in the streamwise. This demonstrates the adequacy of the computational domain in the spanwise direction. Although a slight narrowing is noted in the pressure correlation (when compared with streamwise separation), the difference is quite small when compared with the velocity structures.

Up until a separation of $|r_y/\delta| < 0.125$, the streamwise and spanwise correlations map quite well on top of one another. All velocity structures show regions of negative correlation. The presence of these regions (most notably in the spanwise and vertical correlations) suggests the existance of vortical structres that are aligned in the streamwise direction. Interestingly, the steamwise correlation shows negative correlation at large separation distances after a large region of zero correlation.

Figure 4b shows the one-dimensional spanwise correlation in the far field. All results show a broadening of the structures with an increase in distance from the wall.

VI. Two-Dimensional Correlations

We now present velocity and pressure correlations as functions of two variables, effectively, looking at the average cross-section of a turbulent structure. Presented here are three different planes of interest: $x/y \rightarrow R_{ab}(\Delta x, \Delta y, z_1, z_1)$, $x/z \rightarrow R_{ab}(\Delta x, 0, z_1, z)$, and $y/z \rightarrow R_{ab}(0, \Delta y, z_1, z)$.

A. Horizontal Projections

Shown in Fig. 5 is the $R_{u'u'}$ correlation. For comparison, contours of the u' fluctuating velocity component are also shown at the corresponding horizontal plane. Figure 5a demonstrates some elongated structures that are slightly inclined from the positive r_x axis. The autocorrelation also indicates the elongated and inclined structure shown in the velocity perturbation image. The tilt in the autocorrelation is a biproduct of the Coriolis effect as nonrotating boundary layers would exhibit no such inclination. It was determined that the angle corresponds to the direction of the local shear stress.

Away from the wall (Figs. 5b and 5d), the streamwise correlation still shows a preferred orientation for large spacing which is roughly aligned with the streamwise direction. The contours, however, are slightly angled in the opposite direction than in the near wall contours for both the instantaneous results as well as the two-point correlations.

Similarly, the x/y projection of the v' two-point correlation is provided in Fig. 6. As with the streamwise component, the structures are characterized by streaky structures aligned with the local shear near the wall. Regions of slight negative correlation are evident with moderate spanwise spacing. Away from the wall the alignment of the two-point correlation has shifted such that the structure aligns with its corresponding velocity component r_y. Although not included here, moving further into the boundary layer continues this trend until the v' is stretched only in the spanwise direction.

The vertical velocity two-point correlation in the x/y plane is presented in Fig. 7. The most striking feature of the structure is the much smaller scale than the results already presented. The domain is clearly adequate to capture the entire autocorrelation. Once again, the flow is characterized by streaky structures aligned with the mean shear. The vertical correlation shows strong region of negative

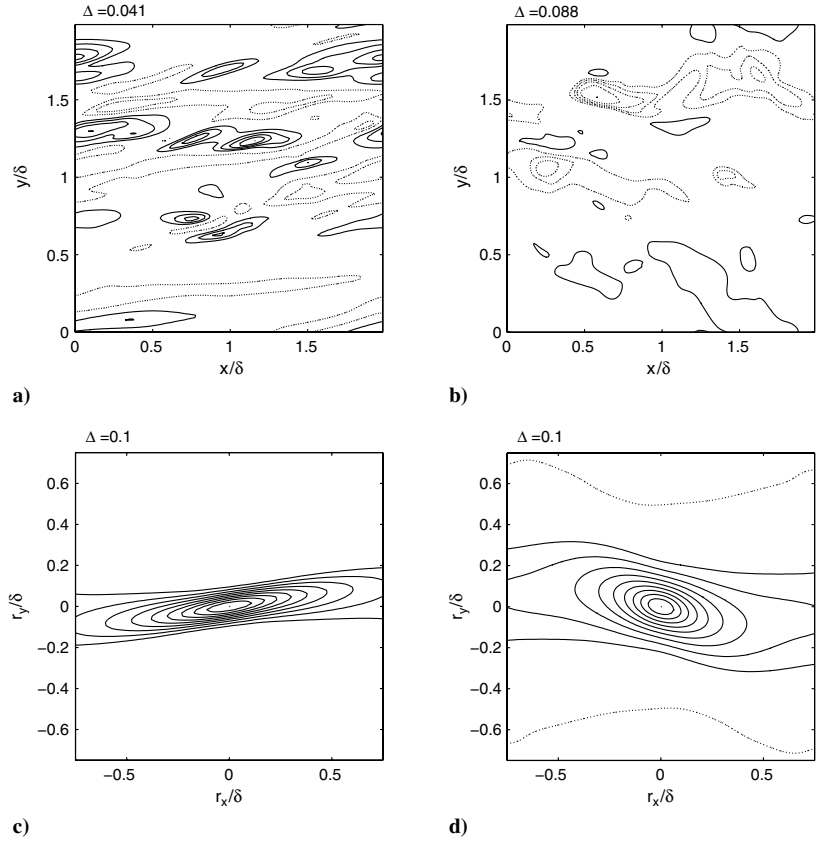

Fig. 5 x/y **projection of** u'**: positive (solid line) and negative (dotted line); parts a and c)** $z_1^+ = z_2^+ \approx 2.60$**, and parts b and d)** $z_1^+ = z_2^+ \approx 88.16$**.**

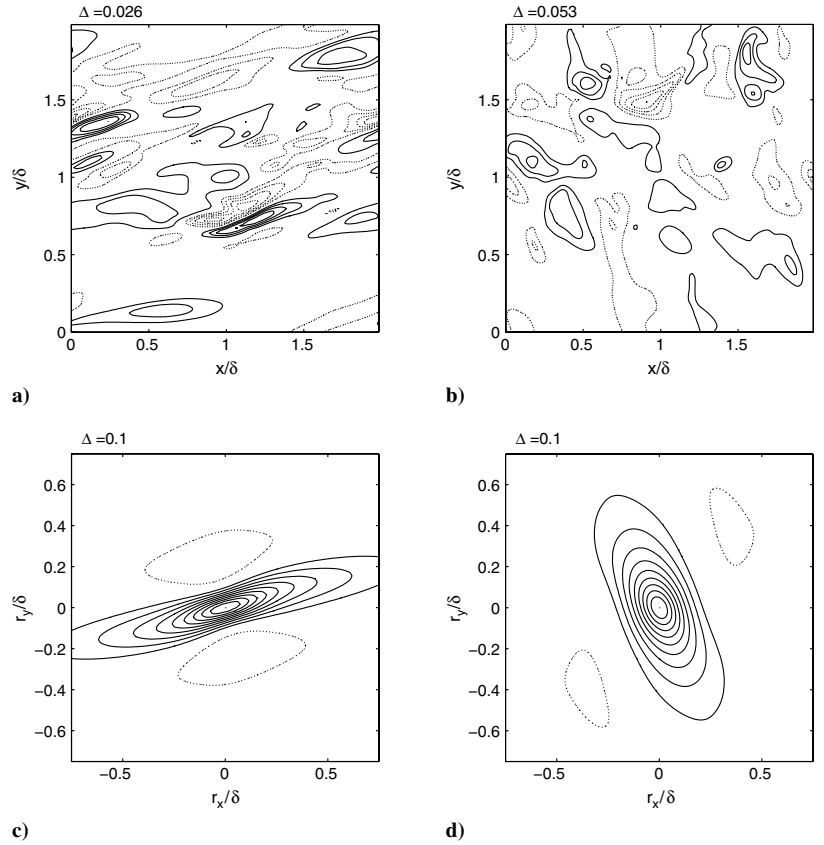

Fig. 6 x/y **projection of** v'**: positive (solid line) and negative (dotted line); parts a and c)** $z_1^+ = z_2^+ \approx 2.60$**, and parts b and d)** $z_1^+ = z_2^+ \approx 88.16$**.**

correlation in the cross-shear direction. Moving away from the wall, the w' two-point correlation shows no preferred direction as the contour becomes circular. The lack of negative correlation suggests that vortical structures exist only in the near wall region. Since both the u' and v' correlations showed stretching in the direction of the velocity, it can be speculated that the same result will be seen for the w' results when viewing a x/z or y/z projection.

The pressure two-point correlation is presented in Fig. 8. At first glance the results seem similar to those of the previous velocity correlations. However, there are small difference that can be noted. First, looking at Fig. 8c, the structure appears to be aligned with the local shear stress. However, comparing this result with the previous velocity correlations we can see that the angle of the contours is increased slightly over the other results. Additionally, the contours remain roughly circular until $R_{p'p'}$ is approximately less than 0.5. This result compliments those shown in Figs. 3 and 4 where little variation is shown between directions near the wall.

Away from the wall (Fig. 8d), the correlation remains inclined at nearly the same angle as the contours close to the wall. Thus the pressure structure is affected relatively little by the distance from the wall.

B. Streamwise Projections

To gather an understanding of how the turbulent structures are affected by the wall we will now analyze the vertical projections of the instantaneous flowfield and the two-point correlations. The correlations give a general idea of the shape of a turbulent structure centered at an arbitrary z_1. By looking at contours for varying z_1 it is possible to determine how a structure evolves as it moves from the viscous region into the outer layer.

Presented in Fig. 9 is a snapshot of the turbulent field at $y/\delta = 0$. For brevity, additional contours for different y/δ have been omitted. Since the problem definition has no dependence on x or y, choosing to show results at this specific location is representative of the turbulent structures at any other plane. Note that the vertical scale is magnified by a factor of two so that near wall features can be seen. The streamwise fluctuating velocity shown in Fig. 9a is characterized by strong gradients in the vertical direction close to the wall. As was seen in Fig. 5c, the structures appear to be elongated in the x direction. The spanwise velocity contours show noticeable lifting with increased x/δ. The structures also are stretched in the vertical direction further into the boundary layer. An interesting characteristic occurs for the spanwise velocity at $0.2 \leq z/\delta \leq 0.4$. Moving across the streamwise separation we see an alternating pattern of positive and negative perturbations. Although this is only one individual snapshot, other projections displayed the same pattern. Little can be gathered from the vertical velocity contours although it does appear that there is slight vertical stretching in Fig. 9c. The fluctuating pressure contours shown in Fig. 9d lead us to believe that the largest gradient of pressure fluctuations is in the streamwise (and spanwise) direction. Consequently, there is noticeable stretching of the contours in the vertical direction.

Figure 10 displays two-point correlations defined by $R_{ab}(\Delta x, 0, z_1, z)$ for $z_1^+ = 2.60$. The streamwise correlations $R_{u'u'}$ (Fig. 10a) show stretching of the streamwise contours in the x direction as is expected at this location. $R_{v'v'}$ contours (Fig. 10b) indicate lifting in the downstream region of the flowfield coupled with a region of negative correlation extending higher in the boundary layer and slightly upstream of the positive correlation region. The $R_{w'w'}$ contours show little stretching in any direction. All three velocity components show a degree of disconnect from the overlying flow. However, the pressure two-point correlation contours (Fig. 10d) display vertical stretching and a sharp gradient in the streamwise direction.

Results for $z_1^+ = 88.16$ are shown in Fig. 11. $R_{u'u'}$ contours show no vertical stretching and only a small region of negative correlation. The v' correlations indicate an increase in the vertical stretching (when compared with results when $z_1^+ = 2.60$). The lifting that was previously noted has transformed into a noticeable tilt in the correlation with a negative region below and downstream of the focus.

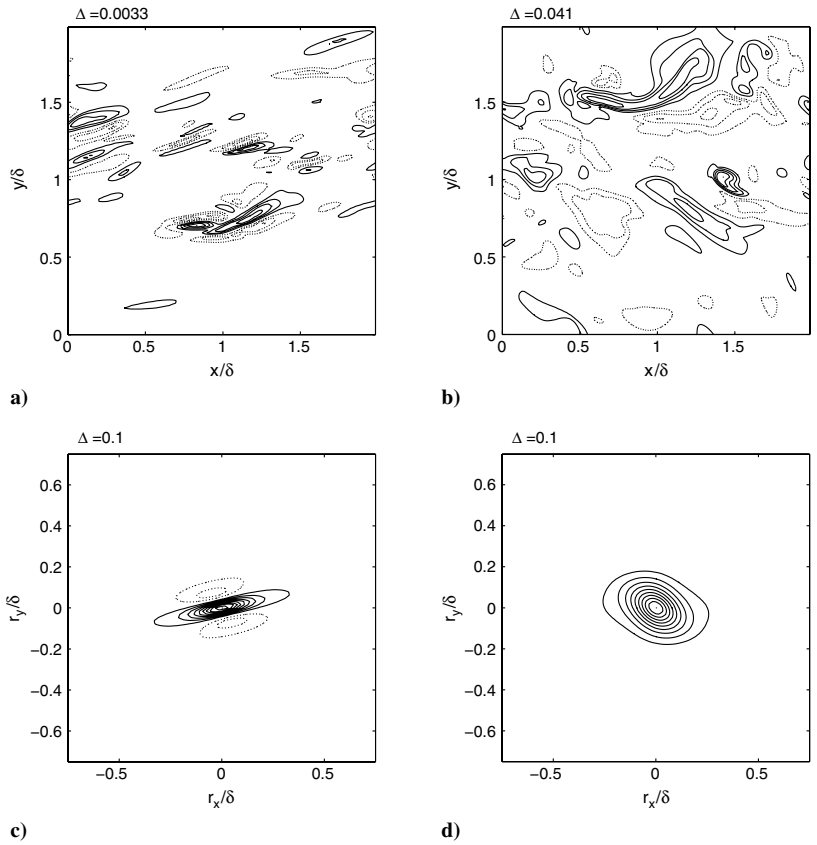

Fig. 7 x/y projection of w': positive (solid line) and negative (dotted line); parts a and c) $z_1^+ = z_2^+ \approx 2.60$, and parts b and d) $z_1^+ = z_2^+ \approx 88.16$.

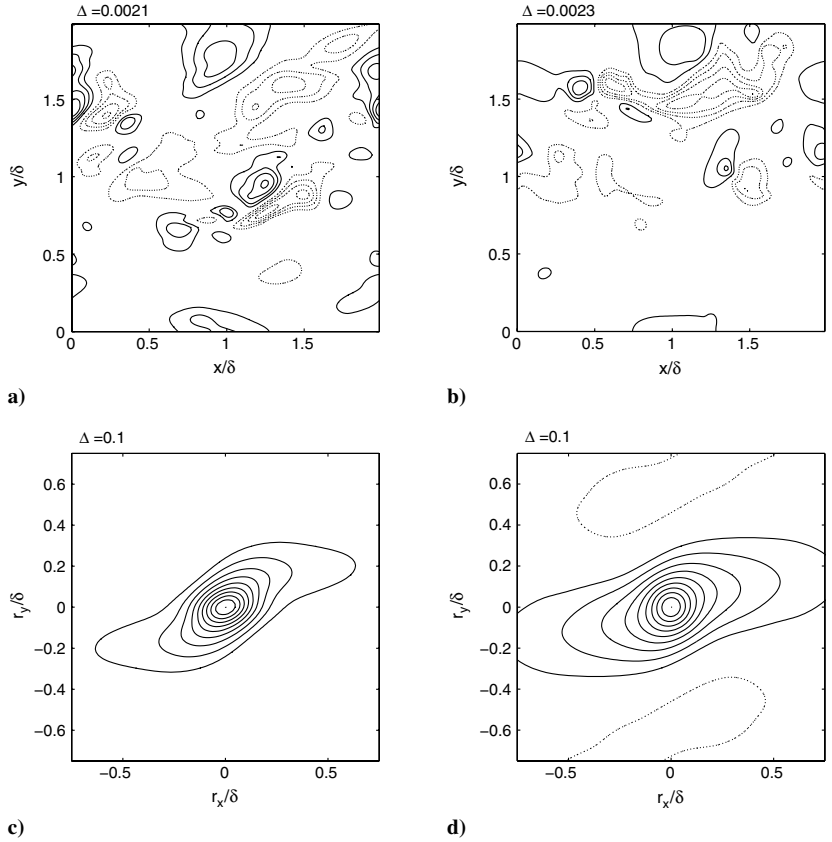

Fig. 8 x/y **projection of** p'**: positive (solid line) and negative (dotted line); parts a and c)** $z_1^+ = z_2^+ \approx 2.60$**, and parts b and d)** $z_1^+ = z_2^+ \approx 88.16$**.**

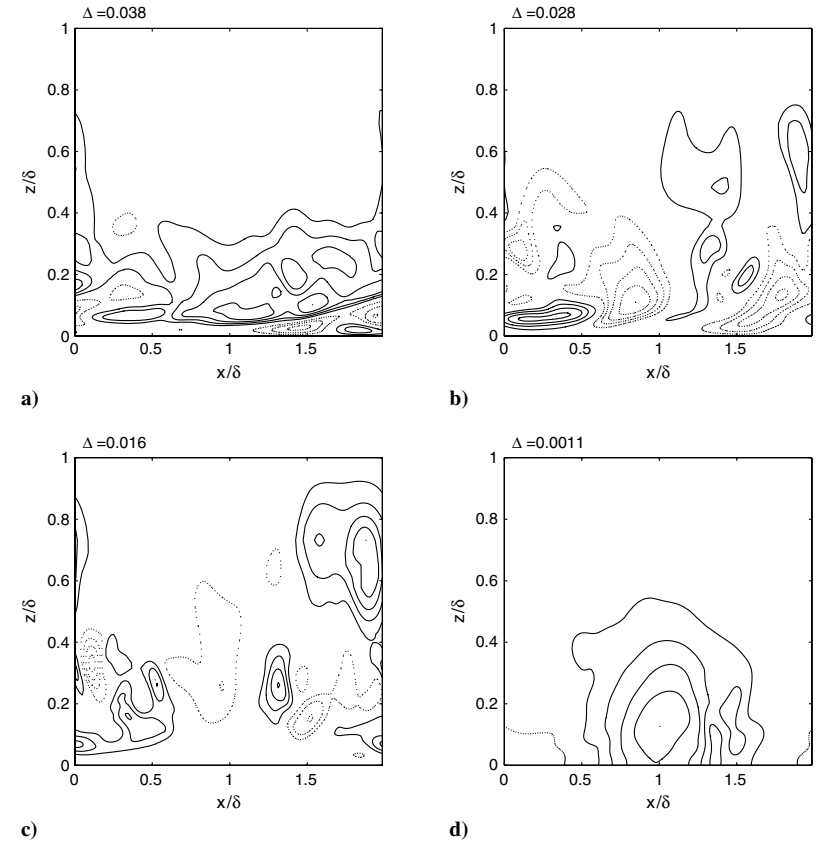

Fig. 9 x/z **projection of field: positive (solid line) and negative (dotted line); a)** u'**, b)** v'**, c)** w'**, and d)** p'**.**

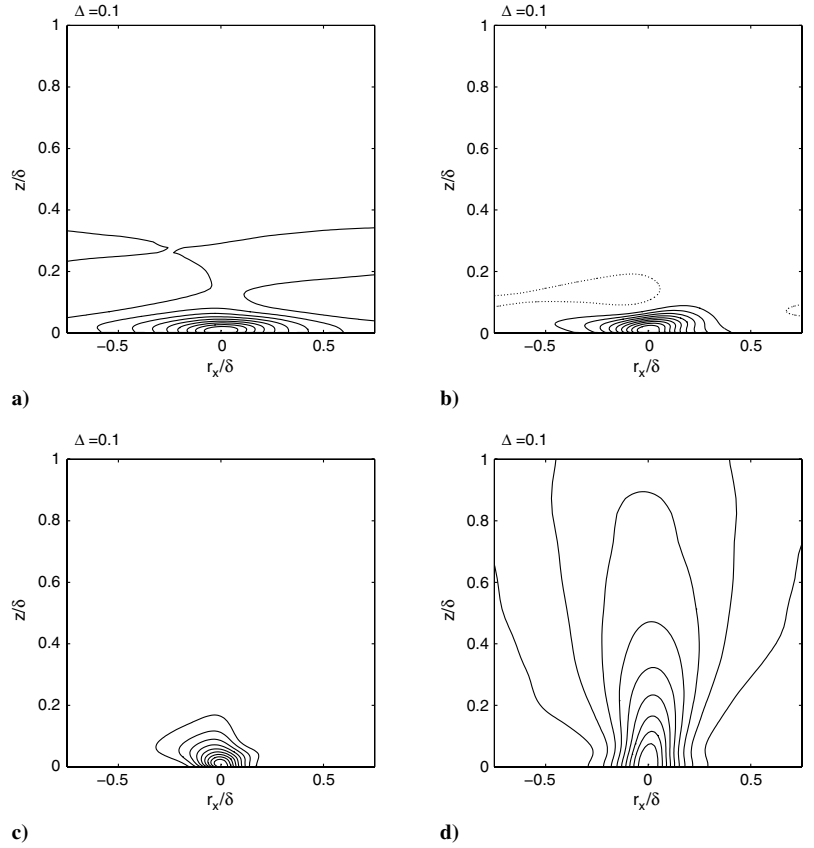

Fig. 10 x/z **projection of two-point correlations,** $z_1 = 2.60$**: positive (solid line) and negative (dotted line); a)** $R_{u'u'}$**, b)** $R_{v'v'}$**, c)** $R_{w'w'}$**, and d)** $R_{p'p'}$**.**

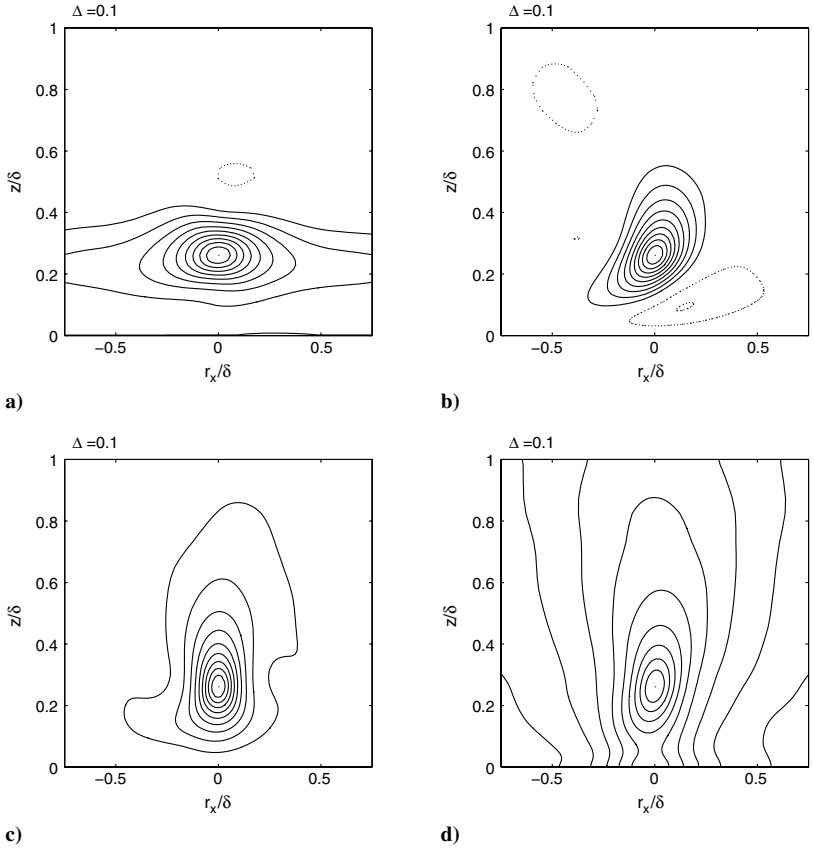

Fig. 11 x/z **projection of two-point correlations,** $z_1 = 88.16$**: positive (solid line) and negative (dotted line); a)** $R_{u'u'}$**, b)** $R_{v'v'}$**, c)** $R_{w'w'}$**, and d)** $R_{p'p'}$**.**

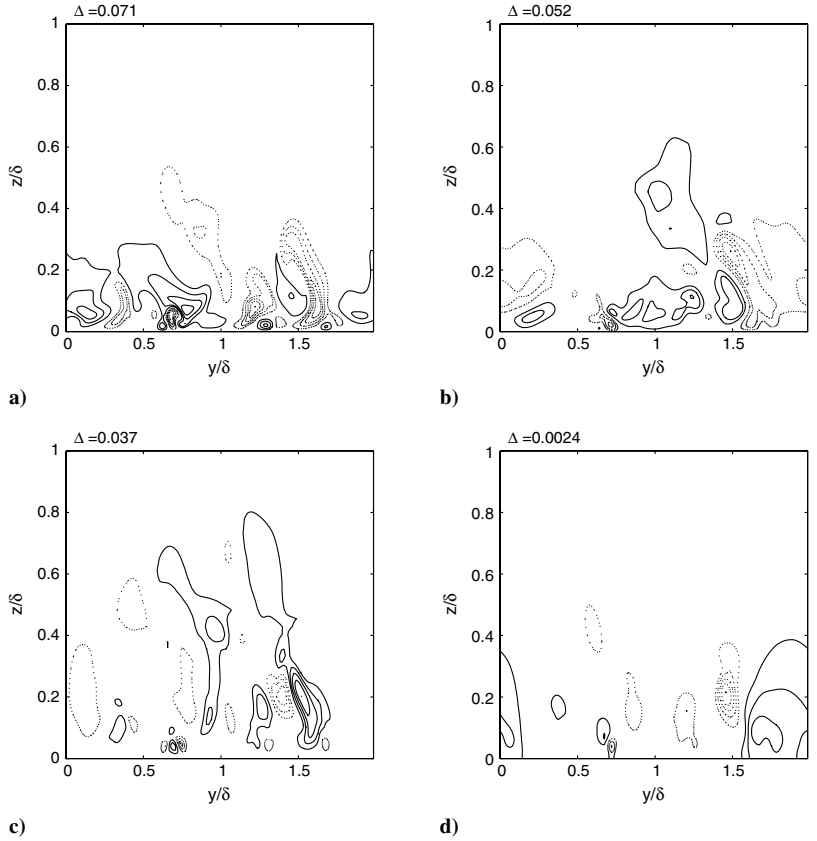

Fig. 12 y/z **projection of field: positive (solid line) and negative (dotted line); a)** u'**, b)** v'**, c)** w'**, and d)** p'**.**

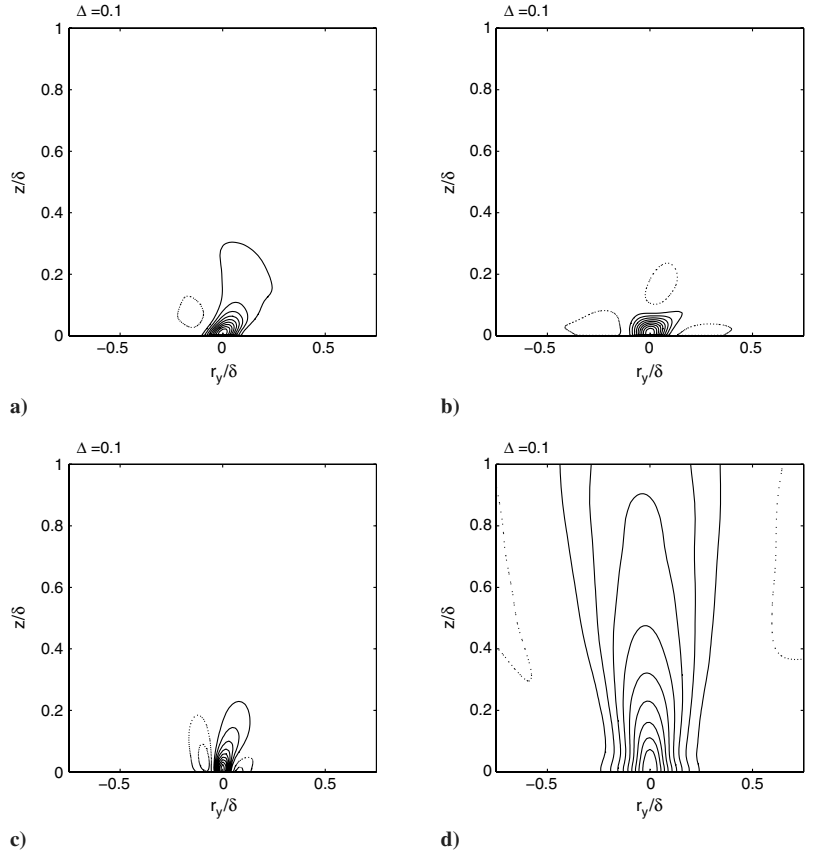

Fig. 13 y/z **projection of two-point correlations,** $z_1 = 2.60$**: positive (solid line) and negative (dotted line); a)** $R_{u'u'}$**, b)** $R_{v'v'}$**, c)** $R_{w'w'}$**, and d)** $R_{p'p'}$**.**

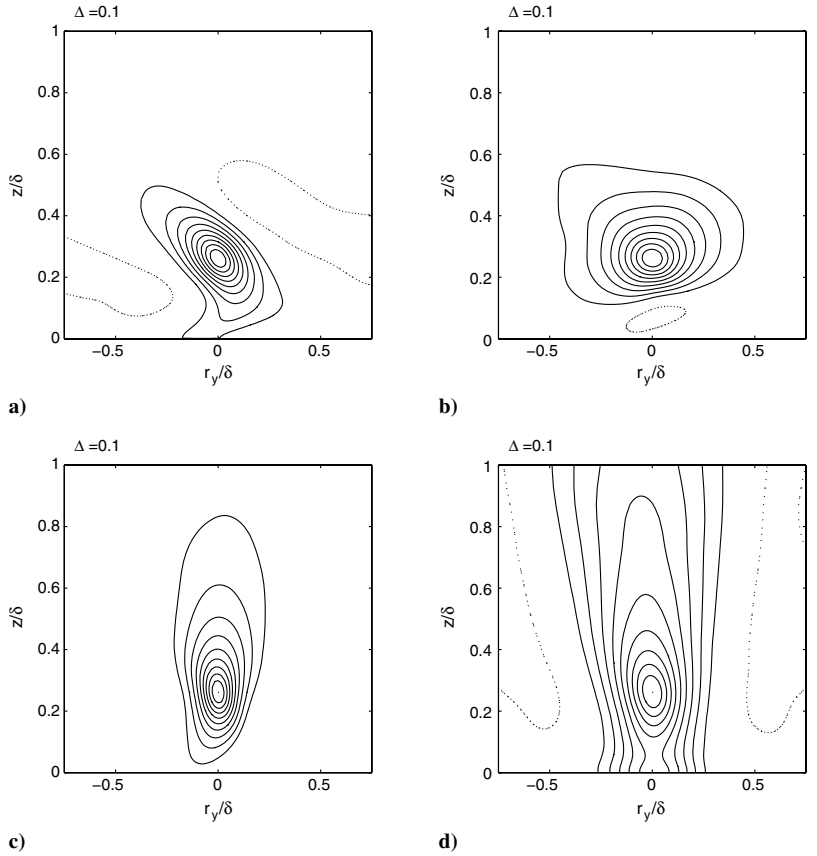

Fig. 14 y/z **projection of two-point correlations,** $z_1 = 88.16$**: positive (solid line) and negative (dotted line); a)** $R_{u'u'}$**, b)** $R_{v'v'}$**, c)** $R_{w'w'}$**, and d)** $R_{p'p'}$**.**

The vertical contours show stretching in the vertical direction with little tilt suggesting that Coriolis force only indirectly affects the vertical velocity. As before, the pressure contours show little variation in the vertical direction.

C. Spanwise Projections

Presented in Fig. 12 are the fluctuating velocity and pressure contours at $x/\delta = 0$. The u' contours in subplot a show a noticeable leftward tilt. Near the surface, the streamwise field is characterized by sharp gradients. The spanwise contours in Fig. 12b also have a slight leftward tilt, though not to the same extent as the streamwise velocity. In Fig. 12c we can see the development of several structures stretched in the z direction.

Figure 13 shows the two-point correlations near the wall with spanwise separation. The streamwise correlation shows a rightward tilt near the wall with opposite tilting away from the wall. A region of negative correlation is located left of the structure. The clear tilting of the structure is a direct effect of the Coriolis forcing. For the spanwise and vertical correlations there are regions of negative correlation on either side of the positive structure. A slight inclination can be found in the spanwise and vertical correlations (Figs. 13b and 13c, respectively) beginning at approximately $z/\delta \approx 0.05$. For the spanwise correlation, this tilt extends into the negative correlation region. The pressure correlation is noticeably narrower than the structure shown in Fig. 10d and includes regions of negative correlation deep in the layer.

Viewing the structures centered away from the wall (Fig. 14), the most noticeable feature is the near constant tilt in the contours for the $R_{u'u'}$ autocorrelation. It is surmised that this tilt is due to the vertical gradient of the mean shear and Reynolds shear stress vectors [1]. This dominant leftward tilt is not noted in any of the other contours presented for spanwise separation. The spanwise contours broaden further from the wall and a slightly tilted region of negative correlation appears under the center of the spanwise correlation. As with the w' velocity contours, the $R_{w'w'}$ correlation tends to align with the direction of the velocity component. Little change is noted between the pressure contours near the wall and further into the boundary layer.

VII. Conclusions

This study investigated one-dimensional and two-dimensional two-point correlations for the turbulent Ekman layer. Results show that the turbulent structures share common traits to nonrotating flows including channel and boundary-layer flows. Near the wall, the structures are elongated in the streamwise direction while aligning with the local shear direction. Broadening in the spanwise direction of the eddies may be attributed to the energy transfer between the vertical fluctuating velocity and the spanwise variances through the return-to-isotropy pressure strain terms [7]. Moving away from the wall the eddies demonstrate downstream lifting characteristic of nonrotating boundary layers. The most notable difference between the turbulent Ekman layer and other boundary layers is apparent in the $R_{u'u'}$ correlation. The opposite tilting evident in the presented contours is attributed to the vertical variation in the direction of the Reynolds stress and mean velocity gradient vectors [1].

Acknowledgments

Support for Scott Waggy provided by the Graduate Assistantship in Areas of National Need Fellowship through the Aerospace Engineering Sciences department at the University of Colorado, Boulder. Support for Stuart Marlatt provided by an Advanced Studies Program sponsored by the University Corporation for Atmospheric Research. We thank Kurt Maute for availing computer resources at the Aerospace Engineering Sciences Center for Aerospace Structures, University of Colorado, Boulder. The authors would like to thankfully acknowledge the support of James C. McWilliams (previously at the National Center for Atmospheric

Research, Boulder). Additional computer time was provided by NSF MRI Grant #CNS-0421498, NSF MRI Grant #CNS-0420873, NSF MRI Grant #CNS-0420985, NSF sponsorship of the National Center for Atmospheric Research, the University of Colorado, and a grant from the IBM Shared University Research program.

References

[1] Marlatt, S., Waggy, S., and Biringen, S., "Direct Numerical Simulation of the Turbulent Ekman Layer: Turbulent Energy Budgets," *Journal of Thermophysics and Heat Transfer*, Vol. 24, No. 3, 2010, pp. 544–555. doi:10.2514/1.45200

[2] Miyashita, K., Iwamoto, K., and Kawamura, H., "Direct Numerical Simulation of the Neutrally Stratified Turbulent Ekman Boundary Layer," *Journal of the Earth Simulator*, Vol. 6, 2006, pp. 3–15.

[3] Le, A. T., Coleman, G., and Kim, J., "Near-Wall Turbulence Structures in Three-Dimensional Boundary Layers," *International Journal of Heat and Fluid Flow*, Vol. 21, No. 5, 2000, pp. 480–488. doi:10.1016/S0142-727X(00)00035-7

[4] Coleman, G. N., "Similarity Statistics from a Direct Numerical Simulation of the Neutrally Stratified Planetary Boundary Layer," *Journal of the Atmospheric Sciences*, Vol. 56, 1999, pp. 891–900.

[5] Taylor, J. R., and Sarkar, S., "Direct and Large Eddy Simulations of a Bottom Ekman Layer Under an External Stratification," *International Journal of Heat and Fluid Flow*, Vol. 29, No. 3, 2008, pp. 721–732. doi:10.1016/j.ijheatfluidflow.2008.01.017

[6] Coleman, G. N., Ferziger, J. H., and Spalart, P. R., "A Numerical Study of the Ekman Layer," *Journal of Fluid Mechanics*, Vol. 213, No. -1, 1990, pp. 313–348. doi:10.1017/S0022112090002348

[7] Marlatt, S. W., "Direct Numerical Simulation of Ekman Layer Transition and Turbulence," Ph.D. Thesis, Univ. of Colorado, Boulder, CO, 1994.

[8] Coleman, G. N., and Ferziger, J. H., "Direct Numerical Simulation of a Vigorously Heated Low Reynolds Number Convective Boundary Layer," *Dynamics of Atmospheres and Oceans*, Vol. 24, Nos 1–4, 1996, pp. 85–94. doi:10.1016/0377-0265(95)00456-4

[9] Le, H., and Moin, P., "An Improvement of Fractional Step Methods for the Incompressible Navier–Stokes Equations," *Journal of Computational Physics*, Vol. 92, No. 2, 1991, pp. 369–379. doi:10.1016/0021-9991(91)90215-7

[10] Marlatt, S., and Biringen, S., "Numerical Simulation of Spatially Evolving Ekman Layer Instability," *Physics of Fluids*, Vol. 7, No. 2, 1995, pp. 449–451. doi:10.1063/1.868642

[11] Pope, S. B., *Turbulent Flows*, Cambridge Univ. Press, Cambridge, United Kingdom, 1993, pp. 182–276.